The Astrophysical Journal, 743:119 (13pp), 2011 December 20 doi:10.1088/0004-637X/743/2/119

OPTICAL POLARIZATION AND SPECTRAL VARIABILITY IN THE M87 JET

Eric S. Perlman[1], Steven C. Adams[2,11], Mihai Cara[1,12], Matthew Bourque[1,3], D. E. Harris[3], Juan P. Madrid[4], Raymond C. Simons[1], Eric Clausen-Brown[5], C. C. Cheung[6,13], Lukasz Stawarz[7,8], Markos Georganopoulos[9], William B. Sparks[10], and John A. Biretta[10]

[1] Department of Physics and Space Sciences, 150 W. University Blvd., Florida Institute of Technology, Melbourne, FL 32901, USA; eperlman@fit.edu
[2] Department of Physics and Astronomy, University of Georgia, Athens, GA 30605, USA
[3] Harvard-Smithsonian Center for Astrophysics, 60 Garden Street, Cambridge, MA 02138, USA
[4] Center for Astrophysics and Supercomputing, Swinburne University of Technology, Hawthorn, VIC 3122, Australia
[5] Department of Physics, Purdue University, West Lafayette, IN 47907, USA
[6] National Academy of Sciences, Washington, DC 20001, USA
[7] Institute of Space and Astronautical Science, JAXA, 3-1-1 Yoshinodai, Chuo-ku, Sagamihara, Kanagawa 252-5210, Japan
[8] Astronomical Observatory, Jagiellonian University, ul. Orla 171, 30-244 Kraków, Poland
[9] Department of Physics, University of Maryland–Baltimore County, 1000 Hilltop Circle, Baltimore, MD 21250, USA
[10] Space Telescope Science Institute, 3700 San Martin Drive, Baltimore, MD 21218, USA
Received 2011 June 15; accepted 2011 September 28; published 2011 November 29

ABSTRACT

During the last decade, M87's jet has been the site of an extraordinary variability event, with one knot (HST-1) increasing by over a factor 100 in brightness. Variability has also been seen on timescales of months in the nuclear flux. Here we discuss the optical–UV polarization and spectral variability of these components, which show vastly different behavior. HST-1 shows a highly significant correlation between flux and polarization, with P increasing from $\sim$20% at minimum to $>$40% at maximum, while the orientation of its electric vector stayed constant. HST-1's optical–UV spectrum is very hard ($\alpha_{\rm UV-O} \sim 0.5$, $F_\nu \propto \nu^{-\alpha}$), and displays "hard lags" during epochs 2004.9–2005.5, including the peak of the flare, with soft lags at later epochs. We interpret the behavior of HST-1 as enhanced particle acceleration in a shock, with cooling from both particle aging and the relaxation of the compression. We set 2σ upper limits of 0.5δ pc and $1.02c$ on the size and advance speed of the flaring region. The slight deviation of the electric vector orientation from the jet position angle (P.A.) makes it likely that on smaller scales the flaring region has either a double or twisted structure. By contrast, the nucleus displays much more rapid variability, with a highly variable electric vector orientation and "looping" in the (I, P) plane. The nucleus has a much steeper spectrum ($\alpha_{\rm UV-O} \sim 1.5$) but does not show UV–optical spectral variability. Its behavior can be interpreted as either a helical distortion to a steady jet or a shock propagating through a helical jet.

Key words: galaxies: active – galaxies: individual (M87) – galaxies: jets – galaxies: nuclei

Online-only material: color figures

1. INTRODUCTION

M87's jet was one of the first observed manifestations of the active galactic nucleus (AGN) phenomenon (Curtis 1918) and has been the target of myriad observations due to its brightness and also proximity ($d = 16$ Mpc; Tonry 1991). During the last decade, M87's jet has been the site of an extraordinary variability event, with knot HST-1 increasing in optical/UV brightness by a factor of more than 100 between 2000 and its peak in 2005. The flare in knot HST-1 has been the target of several monitoring efforts using the *Hubble Space Telescope* (hereafter *HST*), *Chandra X-Ray Observatory*, Very Large Array (VLA), and other telescopes. Previous papers from this project include Paper I reporting our first results (Harris et al. 2003), Paper II which focused on the *HST* data (Perlman et al. 2003), Paper III which was mainly on the X-ray light curve of HST-1 which delineated the massive 2005 flare (Harris et al. 2006), Paper IV which focused on the Very Long Baseline Array (VLBA) results, showing superluminal proper motions in HST-1 (Cheung et al. 2007), and Paper V (Harris et al. 2009) which focused on a more detailed analysis of the variability timescales of HST-1 and the nucleus. Madrid (2009) has also added a complete analysis of the UV light curve of HST-1 and the nucleus between 2000 and 2006.

In this paper (VI of the series), we discuss two additional aspects of the monitoring campaign, namely, the evolution of the polarization and spectral index in the optical–UV. We concentrate on the nucleus and HST-1, as they are the main variable components in the jet. A future paper will combine these observations to produce a new polarization map of the entire jet and discuss any changes over the decade between the data of Perlman et al. (1999) and this paper. Section 2 provides a detailed explanation of the observations and data reduction process. Then, in Section 3, we will discuss the techniques used in reducing the data. In Section 4, we will discuss results. Finally, in Section 5, we discuss implications for jet variability models and close in Section 6 with a summary.

2. OBSERVATIONS

As has been well documented (e.g., Paper I; Waters & Zepf 2005), the flare of knot HST-1 began sometime during 2000. While the jet of M87 was a regular target for *HST* and *Chandra* almost from the start, intensive monitoring by these telescopes began in 2002 (Papers I, II, and III; Madrid 2009).

[11] Southeastern Association for Research in Astronomy (SARA) NSF-REU Summer Intern.
[12] Current address: Physics Department, Case Western Reserve University, 10900 Euclid Ave., Cleveland, OH 44106-7079, USA.
[13] National Research Council Research Associate, resident at Naval Research Laboratory, Washington, DC 20375, USA.

Table 1
Photometry of M87 Components

Date (No.)	Core Fluxes (μJy)				HST-1 Fluxes (μJy)			
	F606W	F330W	F250W	F220W	F606W	F330W	F250W	F220W
2002 December 7 (1)	671 ± 7	305 ± 2	...	146 ± 11	232 ± 2	$231^{a} \pm 2$	...	$141^{b} \pm 6$
2002 December 10 (2)	630 ± 6	305 ± 2	...	146 ± 11	237 ± 2	231 ± 2	...	141 ± 6
2003 November 29 (3)	478 ± 5	...	...	137 ± 11	427 ± 4	...	...	244 ± 7
2004 November 28 (4)	1066 ± 11	475 ± 2	306 ± 14	226 ± 14	970 ± 10	882 ± 4	674 ± 12	631 ± 12
2004 December 26 (5)	1306 ± 13	...	363 ± 10	...	1113 ± 11	...	719 ± 10	...
2005 February 9 (6)	891 ± 9	...	280 ± 9	...	1224 ± 12	...	738 ± 10	...
2005 March 27 (7)	1037 ± 10	...	328 ± 10	...	1404 ± 14	...	903 ± 11	...
2005 May 9 (8)	932 ± 9	446 ± 3	274 ± 9	217 ± 9	1333 ± 13	1209 ± 5	878 ± 14	853 ± 14
2005 June 22 (9)	839 ± 8	...	273 ± 9	...	1150 ± 12	...	877 ± 11	...
2005 August 1 (10)	639 ± 6	...	192 ± 7	...	1117 ± 11	...	664 ± 10	...
2005 November 29 (11)	735 ± 7	349 ± 2	217 ± 8	170 ± 8	1019 ± 10	872 ± 6	604 ± 12	616 ± 12
2005 December 26 (12)	756 ± 8	...	234 ± 8	...	987 ± 10	...	590 ± 9	...
2006 February 8 (13)	631 ± 6	...	201 ± 8	160 ± 8	771 ± 8	...	482 ± 8	469 ± 8
2006 March 30 (14)	780 ± 8	...	232 ± 8	...	656 ± 7	...	404 ± 7	...
2006 May 23 (15)	862 ± 9	372 ± 2	193 ± 7	156.4 ± 7	592 ± 6	488 ± 4	361 ± 7	357 ± 7
2006 November 28 (16)	1370 ± 14	636 ± 3	323 ± 9	...	862 ± 9	720 ± 4	486 ± 10	...
2006 December 30 (17)	1006 ± 10	...	276 ± 9	...	682 ± 7	...	414 ± 7	...
2007 November 25 (18)	1292 ± 17	...	...	...	372 ± 4	...	...	...

Notes.
[a] Observations taken 2002 December 10.
[b] Observations taken 2002 November 30.

Here we review these observations, concentrating on the optical polarimetric part of the campaign.

Optical polarimetry was obtained on a somewhat different schedule than the UV imaging discussed in Madrid (2009). Of the 18 observations obtained between 2002 December and 2007 November, 14 occurred on the same schedule as the imaging observations during 2004 November–2006 December. The other four observations were at roughly yearly intervals before and after this period. Polarimetry was done in two bands, F330W and F606W, with F606W observations being done much more often. Table 1 details the scheduling of these observations, along with other information about the nucleus and HST-1 which will be described later.

The High-Resolution Channel (HRC) of the Advanced Camera for Surveys (ACS) was used to obtain the polarimetry data for 17 of the 18 epochs. The ACS HRC is a single-chip CCD camera, with a plate scale of 0.028×0.025 arcsec pixel^{-1}, corresponding to a field of view of about 28×25 arcsec and yielding diffraction limited resolution of $\approx 0\farcs06$ for the F606W observations, and a Nyquist-limited resolution of $\approx 0\farcs05$ for the F330W observations (see Maybhate et al. 2010). On ACS the polarizing set is comprised of either the POL0V, POL60V, and POL120V filters (used for F606W) or the POL0UV, POL60UV, and POL120UV filters (used for F330W). As the three polarization filters can be selected individually (Maybhate et al. 2010), no change in position or chip was necessary between them. All observations were CR-SPLIT to mitigate the effects of cosmic rays, but dithering was typically not done.

For the final epoch, which occurred after ACS went offline due to an electrical short, the Wide Field Planetary Camera 2 (WFPC2) was used for polarimetry. On WFPC2 the polarizing filter set is comprised of the polarization quad filter (POLQ) quad, which has filters at angles of 0, 45, and 90°. The WFPC2 is a chevron-shaped, four-CCD camera, with three wide-field chips (WF2, WF3, and WF4) and a fine-resolution one (PC1). Its setup is less flexible for polarimetry, as the POLQ quad can only be rotated through 51° (Biretta & McMaster 1997). For this reason, we used the three WF chips. These chips have a plate scale of 0.09965 arcsec pixel^{-1}, leading to a final resolution $\sim 0\farcs2$ set by the Nyquist theorem.

3. DATA REDUCTION

We obtained the data for these observations from the *HST* archive. All data were recalibrated with updated flat field files and image distortion correction (IDC) tables, obtained from the STScI Calibration Database System. Standard techniques were used to recalibrate the data. These methods are described in detail in the instrument handbooks for ACS and WFPC2 (Maybhate et al. 2010; Mobasher 2002). Charge Transfer Error (CTE) corrections were computed using the data found in the ACS Instrument Handbook (Maybhate et al. 2010).

After the data were retrieved, MULTIDRIZZLE was used to combine and cosmic ray reject the images. The alignment of images was refined, assuming the positions of the core and HST-1 as canonical and using TWEAKSHIFTS in IRAF to shift the images to a common frame of reference and correct for geometric distortions using the models in the IDC. This was done because experience with the polarizing filters on both ACS and WFPC-2 has shown that there can be small irregularities in the filters that can cause sources that are far away from one's region of interest to shift apparently as compared to other sources in the field. The procedure was also checked by using only the nucleus as canonical, thus allowing for the possibility of motions in HST-1. Unfortunately, with the short exposure times (typically only 600 s per polarizer) there were few or no globular clusters that could be used for all frames, especially as the chip orientation changed from epoch to epoch. Extensive testing gives us confidence, however, that our procedure successfully and repeatably aligns the images to ± 0.2 pixels. Following MULTIDRIZZLE, the orientation was set so that the y-axis corresponds to north. The final result is a cosmic ray rejected

and geometrically corrected image for each polarizer at each epoch (Fruchter & Sosey 2009).

For the F606W data, it was necessary to subtract galaxy emission before performing photometry and polarimetry. We first created a composite image of the galaxy by drizzle-combining all epochs together, to improve the signal-to-noise ratio (S/N) on the host galaxy. We then modeled the galaxy emission using the ELLIPSE and BMODEL tasks in IRAF. After the model image was computed, it was split into three models to correspond to each polarizer, and subtracted, using the IRAF command IMCALC, from the corresponding drizzled image for each polarizer.

3.1. Polarization Images

Next, the drizzled images from each polarizer were used to create images for Stokes I, Q, and U, along with their errors. For the ACS data, we followed the procedure in the ACS data handbook (Maybhate et al. 2010). For the WFPC2 data, the Stokes images were computed by using the WFPC2 Polarization Calibrator tool.[14] This produces the coefficients needed to compute the Stokes images by using Mueller matrices that describe the pick-off mirror, the polarizer filter, and the various rotations between the optical elements and the reference frames. This tool is accurate to ≈1%–2% (Biretta & McMaster 1997). Both of these procedures yield Stokes U, Q, and I images that are combined in a standard way to produce emission weighted fractional polarization (defined as $P = (Q^2 + U^2)^{1/2}/I$) and electric vector position angle (defined as EVPA $= 1/2 \times \tan^{-1}(U/Q)$) images.

After the Stokes images are found, we accounted for the well-known Rician bias in P (Serkowski 1962) using a Python code adapted from the STECF IRAF package (Hook et al. 2000). This code debiases the P image following Wardle & Kronberg (1974) and calculates the error in polarization PA, accounting for the non-Gaussian nature of its distribution (see Naghizadeh-Khouei & Clarke 1993). In performing this calculation, pixels with (S/N)< 0.1 were excluded outright, and since the debiasing is done with a "most-probable value" estimator, pixels where the most-probable value of P was negative, or above the Stokes I value (i.e., $P > 100\%$) were blanked. This code was first used in Perlman et al. (2006).

3.2. Aperture Photometry and Polarimetry

To obtain fluxes in the Stokes parameters, we performed aperture photometry. For the ACS data, we used two concentric apertures for the core (one with a radius of 11 pixels and the other with a radius of 5 pixels) and one centered on HST-1 with a radius of 11 pixels. The smaller of the two core apertures excludes a knot that emerged from the core in later images, while the larger core aperture includes it. While the two light curves show the same behavior, we use only the smaller aperture in this paper. For the lone WFPC2 data set (epoch 18), we used apertures of 4 pixels radius for both the core and HST-1, and also excluded in each aperture an annular region between 4 and 6 pixels from the other. This alternate procedure was made necessary by the much larger pixels of the WFPC2/WFC chips. For the F606W images, after galaxy subtraction rectangular regions located quasi-randomly throughout the galaxy were used to verify the flatness of the remaining background. A similar strategy was used for the F330W images, where the galaxy contribution was minimal. Aperture correction was done to account for the wide wings of the *HST* point-spread function (PSF). As the nucleus and HST-1 are either unresolved or nearly so, we modeled them as PSFs, using TINYTIM (Maybhate et al. 2010; Bohlin 2007). The aperture corrections were generally 10%–20% in flux, similar to those found by Sirianni et al. (2005); however, our method allowed us to account for the fact that the position of these components varied widely on the chip from observation to observation. Count rates were converted to flux using SYNPHOT, recomputing PHOTFLAM values by assuming a spectral index $\alpha = 0.7$ ($F_\nu \propto \nu^{-\alpha}$), appropriate for most of the M87 jet (Perlman et al. 2001). Typical errors for this procedure are <5%. Finally, we also accounted for Galactic extinction using data from NED,[15] which gives $A_B = 0.096$, as well as standard extinction curves. The resulting fluxes in Stokes I are listed in Table 1, while the fractional polarizations and EVPA are given in Table 2.

High-quality UV photometry of these two components was published recently by Madrid (2009). We have utilized those measurements, albeit with some modifications. Rather than correcting all fluxes to a single wavelength as in the Madrid paper, we have utilized the uncorrected fluxes in both F220W and F250W. This minimizes the number of assumptions and also allows us to make use of all the data in the six epochs where observations were taken in both bands, increasing the accuracy of the measured spectral indices in those epochs and also allowing us to check for significant emission in the Mg II λ2798 line, which falls near the center of the F250W bandpass, but is outside the F220W bandpass (no evidence of this line emission was found). The reader is referred to that paper for reduction steps. We list the resulting fluxes in Table 1. In Table 2, we list the spectral indices $\alpha_{\rm UV-O}$.

Errors were propagated in both data sets using standard techniques. The propagated errors include Poisson errors, an additive noise term (the rms background calculated post-galaxy subtraction) and the readout and discretization noises, as well as an additional 1% term to account for uncertainties in SYNPHOT models (Bohlin 2007). For this analysis, we have ignored errors in the F606W galaxy model. The resulting uncertainties in the Stokes Q and U images are approximately Gaussian in nature, with their values being approximately equal to the sum in quadrature of the individual polarizer image errors. Hence, Gaussian error propagation for P is appropriate for our purposes.

4. RESULTS

Figures 1 and 2 show our results for the total flux, optical–UV spectral index, fractional polarization, and EVPA variations of both the nucleus and HST-1. The total fluxes shown are in the F606W band, while all other panels use all available data. The total flux variations mirror those previously shown for the near-UV by Madrid (2009), showing the very large flare in HST-1 as well as two smaller flares in the nucleus during the same time. Because the large majority of these observations occurred during 2004–2006, when the knot was already very bright, we do not see the full dynamic range of the variability exhibited by knot HST-1 during its flare—nearly a factor 150 at 2500 Å, where its flux increased from 6 μJy in 1999 to a peak of 854 μJy in early 2005. We used our data to measure the distance between the two features, which in all epochs is consistent with 0.885 ± 0.010 arcsec, with no evidence of motion. This sets an upper limit of 1.56 pc (2σ) on positional change of the flux maximum of

[14] http://www.stsci.edu/hst/wfpc2/software/wfpc2_pol_calib.html

[15] NASA Extragalactic Database (http://ned.ipac.caltech.edu).

Table 2
Polarimetry and Spectral Information

No.	Core					HST-1				
	F606W P (%)	F606W EVPA (°)	F330W P (%)	F33OW EVPA (°)	α_{O-UV}	F606W P (%)	F606W EVPA (°)	F330W P (%)	F33OW EVPA (°)	α_{O-UV}
1	3.1 ± 0.3	-79.9 ± 3.12	4.5 ± 0.7	-82.5 ± 4.7	1.50 ± 0.06	40.2 ± 4.0	-65.8 ± 3.0	$34.0^{a} \pm 3.5$	-67.5 ± 3.1	0.07 ± 0.04
2	3.7 ± 0.4	-79.6 ± 3.17	4.5 ± 0.7	-82.5 ± 4.7	1.41 ± 0.04	39.9 ± 4.0	-65.3 ± 3.0	34.0 ± 3.5	-67.5 ± 3.1	0.12 ± 0.04
3	5.5 ± 0.6	-70.3 ± 3.07	...	...	1.23 ± 0.08	39.9 ± 4.0	-51.3 ± 3.0	...	...	0.58 ± 0.03
4	1.4 ± 0.2	-10.4 ± 3.37	13.4 ± 1.5	73.7 ± 3.4	1.54 ± 0.06	23.4 ± 2.3	-58.2 ± 3.0	24.8 ± 2.6	-64.7 ± 3.1	0.32 ± 0.03
5	2.0 ± 0.3	-55.4 ± 3.69	...	...	1.58 ± 0.04	27.7 ± 2.8	-56.9 ± 3.0	...	...	0.57 ± 0.02
6	2.2 ± 0.3	-98.9 ± 3.76	...	...	1.42 ± 0.04	36.7 ± 3.7	-58.4 ± 3.0	...	...	0.66 ± 0.02
7	6.1 ± 0.6	-53.2 ± 3.1	...	...	1.41 ± 0.04	42.5 ± 4.3	-61.5 ± 3.0	...	...	0.57 ± 0.02
8	4.1 ± 0.4	-78.9 ± 3.05	10.0 ± 1.3	-86.8 ± 3.8	1.42 ± 0.04	34.5 ± 3.5	-64.7 ± 3.0	38.1 ± 3.9	-62.7 ± 3.0	0.37 ± 0.02
9	10.7 ± 1.1	-36.0 ± 3.04	...	...	1.37 ± 0.04	32.4 ± 3.2	-63.8 ± 3.0	...	...	0.35 ± 0.02
10	8.6 ± 0.9	-62.0 ± 3.09	...	...	1.48 ± 0.05	36.4 ± 3.7	-60.6 ± 3.0	...	...	0.68 ± 0.02
11	6.6 ± 0.7	-69.1 ± 3.03	10.1 ± 1.4	-77.2 ± 4.0	1.45 ± 0.05	32.6 ± 3.3	-62.2 ± 3.0	29.3 ± 3.0	-62.0 ± 3.0	0.45 ± 0.03
12	4.4 ± 0.5	-90.0 ± 3.26	...	...	1.44 ± 0.05	28.1 ± 2.8	-62.4 ± 3.0	...	...	0.67 ± 0.02
13	2.5 ± 0.3	-69.4 ± 3.24	...	...	1.39 ± 0.07	26.3 ± 2.6	-59.5 ± 3.0	...	...	0.55 ± 0.03
14	2.6 ± 0.3	-71.4 ± 3.7	...	...	1.50 ± 0.05	24.1 ± 2.4	-59.0 ± 3.0	...	...	0.63 ± 0.03
15	1.0 ± 0.1	-1.2 ± 3.91	3.0 ± 1.0	-25.7 ± 9.8	1.63 ± 0.05	20.7 ± 2.1	-62.7 ± 3.0	24.4 ± 2.7	-50.2 ± 3.3	0.47 ± 0.03
16	6.6 ± 0.7	-39.1 ± 3.01	2.0 ± 0.7	-57 ± 10	1.50 ± 0.04	34.9 ± 3.5	-66.1 ± 3.0	34.8 ± 3.6	-64.2 ± 3.1	0.48 ± 0.03
17	10.2 ± 1.0	-46.4 ± 3.04	...	...	1.60 ± 0.04	20.3 ± 2.1	-58.7 ± 3.0	...	...	0.73 ± 0.03
18	6.7 ± 3.0	-130.1 ± 1.30	...	...	...	22.2 ± 3.0	-76.5 ± 0.7	...	...	...

Note. [a] Observations taken 2002 December 10.

HST-1 during the roughly five-year timespan covered by these data.

Comparing Figures 1 and 2 we see that the nucleus and HST-1 display very different characteristics in polarization and spectral index variability. Both display large changes in polarization characteristics during the six-year timespan of our observations. The nucleus is seen to range between 1% and 13% polarization during this time, with the EVPA changing by as much as 90°. HST-1 is much more highly polarized, with its polarization ranging from 20% to 45%, but much less variability (marginally significant at most) in the EVPA, which in our data ranges from roughly $-50°$ to $-75°$, with a typical value of $\sim -62°$, about 7°–8° away from the nominal jet direction of $-69.^{\circ}5$ but rather closer (4°) to the average PA of the radius vector for HST-1 during VLBA observations (Paper IV) of $-66°$. The difference between the two angles is only 1σ for any one point, but in 17 of 18 epochs the EVPA is significantly displaced toward the north from the radius vector, making the difference significant at roughly the 3σ level (see also Section 5.1).

For the most part the polarization characteristics in F330W track the ones seen in F606W. This is true for all epochs for knot HST-1. Thus that knot displays no evidence for frequency-dependent polarization behavior. For the nucleus, however, one epoch shows significant ($>2\sigma$) differences between polarization characteristics in the two bands, namely, 2004 November 28. As can be seen in Figure 1, this difference is highly significant both in P (8σ) as well as EVPA (10σ), and we have eliminated all possible sources of instrumental error in the F330W and F606W data for this epoch. We note that this epoch is very near the peak of a flare in the nucleus; however, this flare does not exhibit a spectrum that is significantly different than surrounding epochs. Unfortunately, the next epoch does not have UV polarimetry so we are unable to comment further on whether any frequency-dependent polarization pattern developed during this flare.

Another perspective can be gained by looking at relationship between flux and fractional polarization. This is done in Figure 3, using the F606W data only. In knot HST-1 (bottom panel), this reveals a strong correlation between total flux and fractional polarization, particularly between 2004 November and 2006 December (epochs 4–17), when the flux variability was dominated by the main part of the flare and the monitoring was most frequent. The other four points represent times where the flux variability was either dominated by or had a significant contribution from smaller scale events. Using only epochs 4–17, a Spearman's rho-test indicates $\rho = 0.842$ and $P = 1.6 \times 10^{-4}$. Inspection of the F330W data shows they also follow this correlation. During this time the EVPA is nearly constant (Figure 1), although there is possible evidence for a quasi-sinusoidal modulation. This gives the clear impression of the variability being dominated by a single component with a highly ordered magnetic field. We discuss the implications further in Section 5.2.

A pattern is much more difficult to pick out for the nucleus. We have therefore added red arrows to Figure 3 to guide the eye during the part of the campaign where there is evidence of a pattern. During epochs 6–15, there was a coherent increase and then decrease in the fractional polarization of the nucleus, at a time when the flux variations were small (Figure 1). This translates into a near-vertical "loop" in the polarization-flux plane (Figure 3, top panel), with the initial increase in polarization being correlated with the decrease in flux from epoch 5's maximum, and then a nearly monotonic decrease being observed over epochs 9–15 while the flux varied by only 25%. This is discussed further in Section 5.3.

Table 2 and Figures 1–2 also describe the evolution of the UV–optical spectral index α_{UV-O}. As can be seen, α_{UV-O} behaves differently for the nucleus than it does for HST-1. For the core, we do not see significant variability in the optical spectral index. By contrast, the spectral index is strongly variable for HST-1. For most of the time, the variability of the spectral index appears uncorrelated with flux, but during the brightest part of the flare (epochs 4–9, denoted on Figure 4 by red arrows), we see that the spectral index is larger (i.e., steeper) when the flux is higher. As can be seen in Figure 4, during this time HST-1 describes a definite "loop" in the flux-spectral index plane. This pattern has been called "hard lags" in the blazar and optical

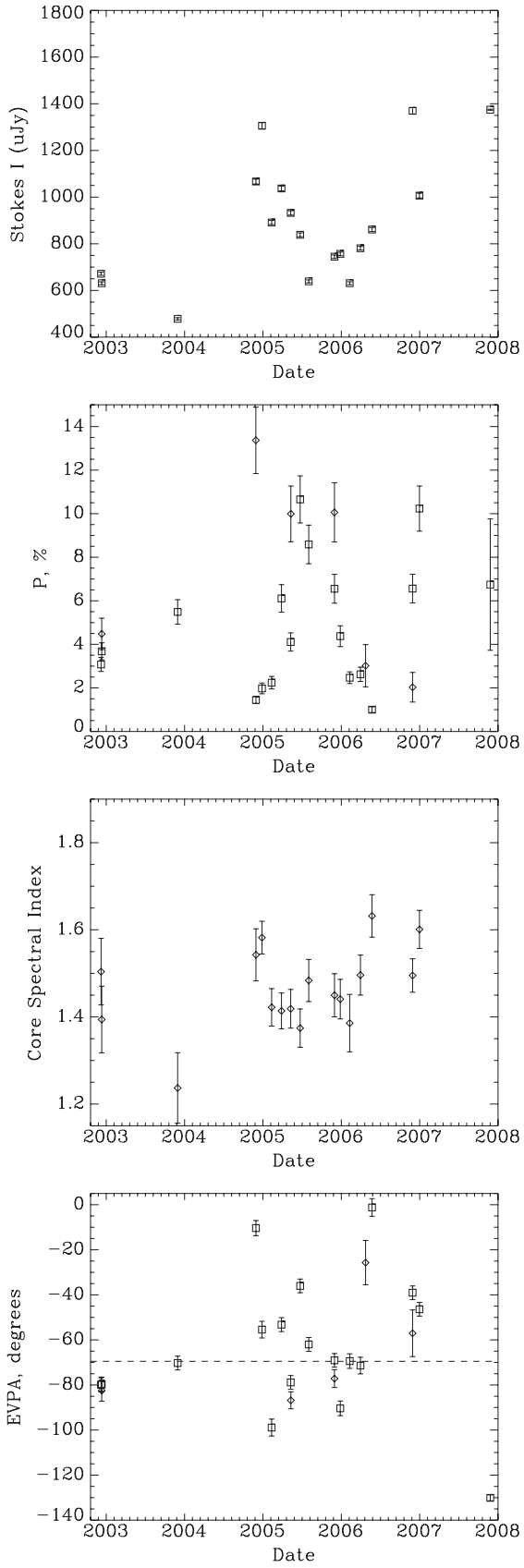

Figure 1. Variations in total flux (i.e., Stokes *I*), fractional polarization, spectral index and EVPA, are plotted for the nucleus of M87. A dashed line in the EVPA panel reflects the jet PA. The F606W observations are plotted as squares, while in the second and fourth panel the F330W polarimetry is plotted as diamonds. See Sections 3.2 and 4 for discussion.

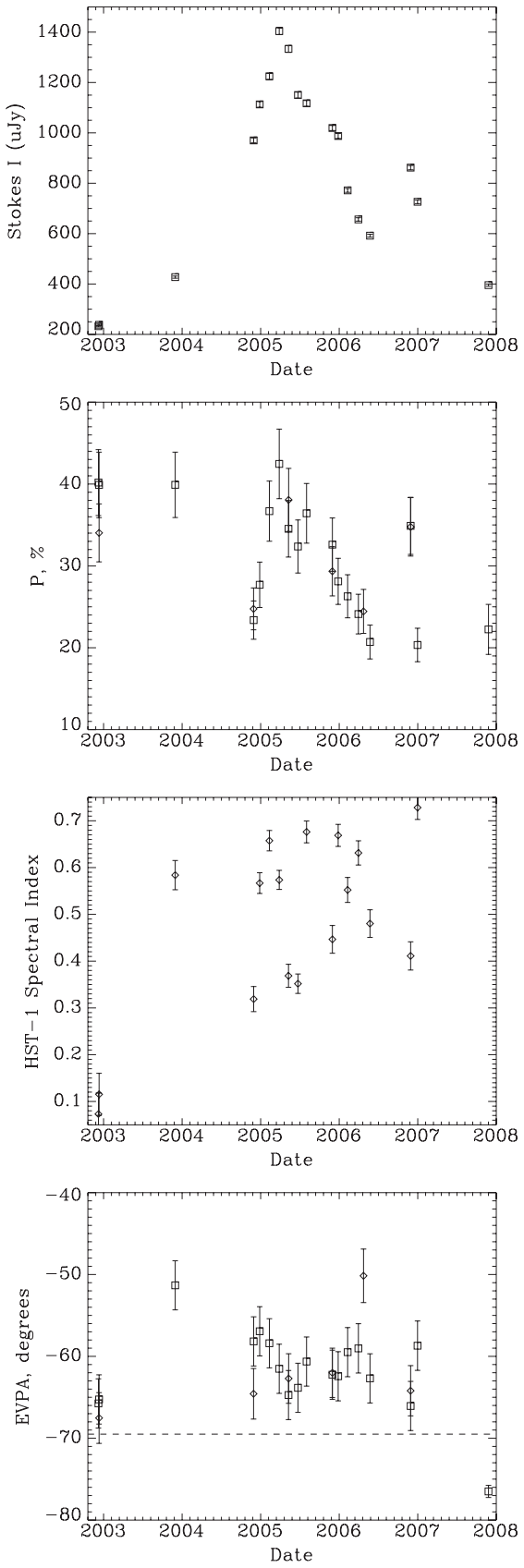

Figure 2. Variations in total flux, fractional polarization, spectral index, and EVPA, are plotted for knot HST-1. A dashed line in the EVPA panel reflects the jet PA. The F606W observations are plotted as squares, while in the second and fourth panel the F330W polarimetry is plotted as diamonds. See Sections 3.2 and 4 for discussion.

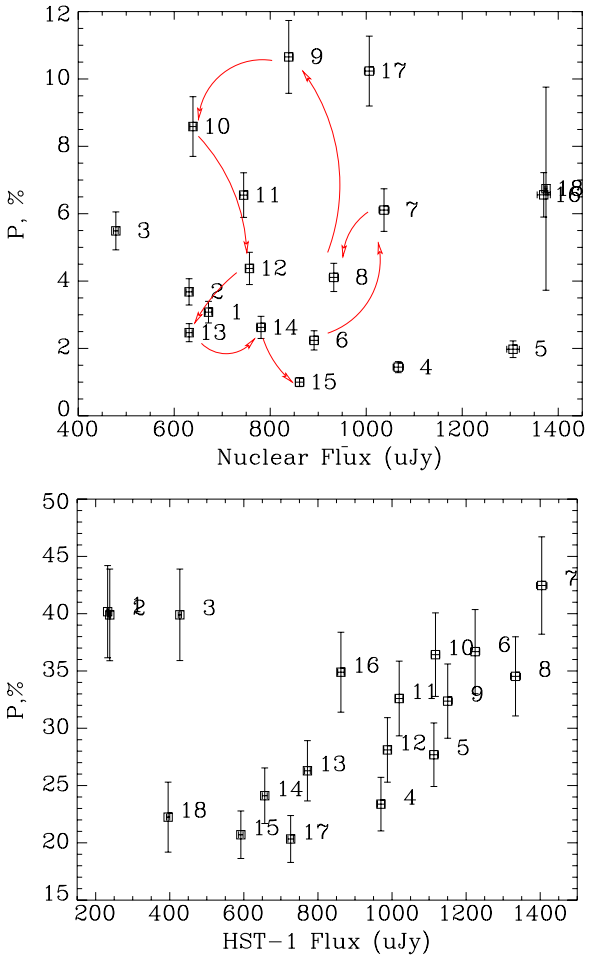

Figure 3. Graphs of fractional polarization versus flux for the core (top) and HST-1 (bottom). The observation epochs have been labeled sequentially. Note that for HST-1, epochs 4–18 display a very strong correlation between the flux and polarization, whereas the behavior for the nucleus is very different, with a "loop" seen between epochs 9–15, but otherwise no organized pattern.

(A color version of this figure is available in the online journal.)

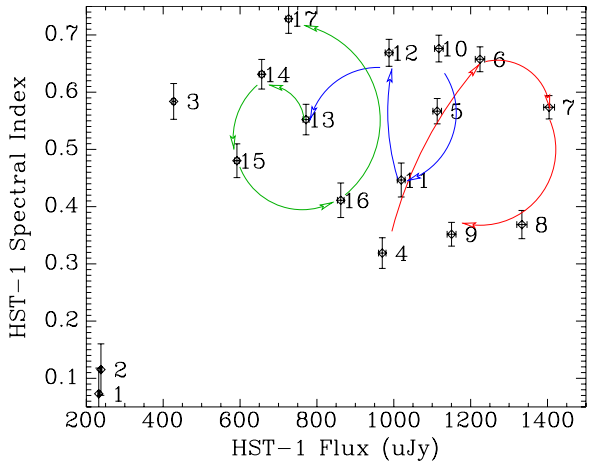

Figure 4. Evolution of α_{UV-O} versus flux for knot HST-1. Each epoch has been labeled sequentially, as in Figure 3. Note the strong "looping" behavior during the maximum of the flare in HST-1, as well as after (green and red arrows). See Sections 4 and 5.1 for discussion.

(A color version of this figure is available in the online journal.)

variability literature (see, e.g., Zhang 2002; Zhang et al. 2002; Fiorucci et al. 2004; the term "counterclockwise looping" is also in use, but note that those papers use the opposite sign convention for α than we do). Looping in the other direction is seen for epochs 13–17 (denoted on Figure 4 by green arrows), e.g., "soft lagging" (Zhang et al. 2002), with oscillations in the plane in between (denoted on Figure 4 by blue arrows). Both "looping" patterns are known to arise for particular relations between the acceleration and cooling timescales controlling the spectral evolution of the radiating particles (in the framework of simplified models for such an evolution) and are discussed further in Section 5.2.

5. DISCUSSION

It is interesting to explore further the reasons behind the highly disparate behaviors of the nucleus and HST-1, as seen in our data as well as other bands. X-ray variability of the nucleus and HST-1 was studied in Papers I, III, and V. Variability has also been seen at gamma-ray energies, where M87 has been detected in both TeV (Aharonian et al. 2003) and GeV (Abdo et al. 2009) energies (although, n.b., in the gamma rays the M87 nucleus and jet cannot be resolved from one another). During the peak of the flare of HST-1 in 2005 March–May, TeV variability on timescales of a few days (Aharonian et al. 2006) was seen, leading Stawarz et al. (2006) to associate the enhanced TeV emission seen in 2005 with the flare of HST-1. However, the origin of other features in the TeV light curve is unclear. A major work compiling all multi-wavelength and TeV gamma-ray variability data for M87 was recently completed by Abramowski et al. (2011). That work concluded that while it remains plausible that both the unresolved nucleus and HST-1 contribute to the TeV emission observed from M87 system during the quiescence epochs and also the 2005 flare, during the 2008 and 2010 epochs of the enhanced γ-ray activity of the source the nucleus is more likely to have contributed the majority of the TeV flux.

In the radio, both Paper IV as well as Chen et al. (2011) studied the variability of knot HST-1, with Paper IV using VLBA data, while Chen et al. (2011) used data from the VLA, both from roughly 2003–2007. The latter work has angular resolution comparable to *HST* and includes an analysis of polarization data, and finds a variable P, EVPA, and rotation measure, as well as a radio spectrum that softened when the knot was brighter. It is difficult to compare their data to ours in detail because Chen et al. (2011) used a subset of the available data, including only four data sets between 2004 and 2006 (and none in 2005), when HST-1 was most active. However their findings, while consistent with the idea of non-cospatial radio and optically emitting particle populations (Perlman et al. 1999), are difficult to reconcile with the much longer radiative lifetimes of radio synchrotron emitting particles, as well as the similar radio and UV light curves.

To further explore the physical implications of our results, it is necessary to discuss the physics of shocks and other disturbances in jets, which may explain the behavior we see. As will be seen, we do this because we believe that both behaviors may be explained by such disturbances. Following this, we will then present physical interpretations of the behaviors of knot HST-1 and the nucleus.

5.1. Shocks, Helical Distortions, and Polarization Variability

The behaviors we see in both the nucleus and HST-1 are direct reflections of the physics in the emitting region. Since the data we have analyzed in this paper includes fluxes, optical–UV

spectra and also polarimetry, we have information both on the interplay between particle acceleration and cooling, as well as the magnetic field structure that was either associated with this behavior or produced it. In order to motivate the discussion herein, it is useful to summarize the commonalities in the behavior of both regions and then discuss why those commonalities argue for an origin in shocks and waves. Both HST-1 and the nucleus exhibit coherent patterns in the (I, P) plane. In the case of HST-1 the pattern is simple: polarization is correlated strongly with intensity, while at the same time the EVPA remains essentially constant very close to the PA of the jet. By comparison, in the nucleus we see a "loop" in the (I, P) plane, with somewhat more complicated EVPA behavior, featuring wild swings of up to 100°, albeit around a dominant orientation that is once again near the PA of the jet's radial motion vector. The fact that both HST-1 and the nucleus display coherent variability patterns in (I, P) while maintaining a single, dominant orientation of EVPA indicates that in both regions, the details of the local magnetic field structure are tightly related to the efficiency of the particle acceleration. That component must have a reasonably well-ordered magnetic field structure, particularly in the case of HST-1 because of its very high polarization (see Section 5.2 for further elaboration on this issue). These behaviors are all consistent with having been produced through shocks and/or waves, although the details of the physics may be different in the two regions.

What types of shocks may be consistent with these behaviors? Perhaps the simplest type of shock to discuss is localized, planar, and oriented along or near the jet perpendicular. This type of model, often known as a "Laing sheet" due to the fact that shocks of this type characteristically compress an initially random magnetic field into a thin sheet with magnetic field along the sheet, has been investigated extensively in the literature, particularly in Laing (1980), Hughes et al. (1985), and Kollgaard et al. (1990). In this model, the properties of a relativistic shock can be completely determined by a few factors. Primary among these is its compression ratio, $k = \Gamma_d\beta_d/(\Gamma_u\beta_u)$ (Laing 1980; Wardle et al. 1994), where $\Gamma_{u,d}$ is the bulk Lorentz factor and $\beta_{u,d}$ is the bulk speed with the subscripts referring to upstream and downstream quantities, respectively. One can also think of the compression ratio in terms of the compression of a unit length. Ignoring the plasma magnetization, the shock jump conditions relate the upstream and downstream speeds via $\beta_u\beta_d = 1/3$ (Landau & Lifshitz 1987) for a plasma with a fully relativistic equation of state. The other factors that describe the shock are the spectral index α, Doppler factor δ, and viewing angle θ_{ob}. More specifically, in this model, Kollgaard et al. (1990) found that the degree of polarization is given by (their Equation (2); note that our convention for the spectral index α is the opposite of the one in Kollgaard et al.):

$$P = \frac{3+3\alpha}{5+3\alpha}\frac{\delta^2(1-k^2)\sin^2\theta_{ob}}{2-\delta^2(1-k^2)\sin^2\theta_{ob}}. \quad (1)$$

This model is obviously dependent on the geometry chosen for the jet magnetic field and for the shock—in particular ignoring any helical component to the field and a strong, perpendicular shock. Such a model can easily produce a correlation between flux and polarization, along with a roughly constant EVPA parallel to the jet direction, as seen in knot HST-1. We will discuss in Section 5.2 the application of this model to HST-1.

If, however, a different type of disturbance is envisioned, quite different polarization behavior can be produced. The first possibility we will consider is a time-varying upstream speed, β_u. This is supported by the variable superluminal speeds observed in AGN jets (e.g., Lister et al. 2009). In this second model, the varying β_u is related to the downstream flow speed via $\beta_u\beta_d = 1/3$ which induces variability in the shock compression factor, k. To induce a variation in the shock compression factor, the stochastic variation in β_u is modeled as being sinusoidal:

$$\beta_u(t) = \beta_{u,0} + A_\beta \sin(\omega_\beta t - \phi_\beta). \quad (2)$$

The parameters ($\beta_{u,0}$, A_β, ω_β, ϕ_β) are free parameters of the model and t is time. If the jet contains a disordered field component B_r, no ordered toroidal field, and an ordered poloidal field B_p, then the polarization depends on the magnetic field through the ratio $\xi = |B_p/B_r|$. Since the process of transforming an initially ordered large-scale field to a tangled one is probably governed by the kink instability (Spruit et al. 1997; Begelman 1998; Marscher 2009), it is natural to assume that the value of ξ at the shock fluctuates in time. Similar to β_u, we model the ξ variation as

$$\xi(t) = \xi_0 + A_\xi \sin(\omega_\xi t - \phi_\xi). \quad (3)$$

The parameters (ξ_0, A_ξ, ω_ξ, ϕ_ξ) are free parameters of the model and t is time. Equations (2) and (3) allow the calculation of the post-shock intensity, I, and polarization P (e.g., Kollgaard et al. 1990):

$$I \propto \delta_d^{2+\alpha} k^{-2} B_r^2 \{2 + [3k^2\xi^2 - (1-k^2)]\sin^2\theta'_{ob}\} \quad (4)$$

$$P \approx \frac{3+3\alpha}{5+3\alpha}\frac{\delta^2[(1-k^2) - 3k^2\xi^2]\sin^2\theta_{ob}}{2-\delta^2(1-k^2)\sin^2\theta_{ob} + 3\delta^2\xi^2k^2\sin^2\theta_{ob}}. \quad (5)$$

Note that Equation (4) is an approximation as it results from integrating over the line of sight with α set to unity for convenience (Wardle et al. 1994), and that Equation (5) as expected reduces to Equation (1) for $\xi = 0$. The downstream Doppler factor, $\delta = (\Gamma_d - \Gamma_d\beta_d\cos\theta_{ob})^{-1}$, raised to the power $2+\alpha$ consistent with a steady jet (Lind & Blandford 1985), is included in the expression for intensity since the flow speed varies in the emission region which is downstream of the shock. In our convention, the EVPA is parallel to the jet axis for $P > 0$ and is perpendicular to it for $P < 0$. The factor B_r^2 in Equation (4) is held as constant in our model. Otherwise, if used as another time-varying parameter, it would merely modify the amplitude of the intensity fluctuations.

Another plausible configuration is one where the jet contains a significant helical component to its magnetic field. Such a scenario might be particularly operative in the nucleus, since AGN jets are generally thought to be launched and collimated within the central $\sim$ parsec by magnetic fields that dominate other sources of pressure. Its applicability to regions further from the nucleus is less certain because it is not known how far downstream from the launching site the jet retains a magnetically dominant ordered helical field since jets are thought to be unstable to the $m = 1$ kink mode (Narayan et al. 2009; Marscher 2009; Spruit 2010). Despite this theoretical uncertainty, some observational evidence suggests that jets contain helical magnetic fields on parsec scales: parsec-scale bulk acceleration (Vlahakis & Königl 2004), Faraday rotation gradients (Asada et al. 2002; Gabuzda et al. 2004; Zavala & Taylor 2005; Kharb et al. 2009), and observed asymmetries in the transverse profiles of polarization, brightness, and spectral index (Clausen-Brown et al. 2011).

Let us assume that a component in the jet contains a large-scale helical magnetic field that is variable due to the growth

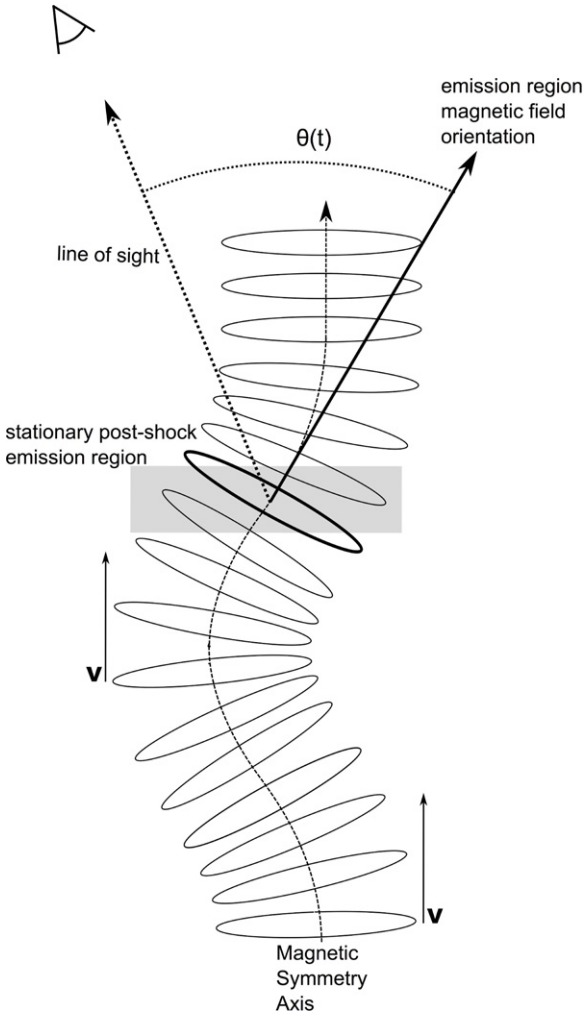

Figure 5. Schematic of the helical distortion model illustrated with toroidal loops of magnetic field. As shown by the velocity vectors (labeled by **v**), the velocity field is uniformly directed despite the kinked jet. As the kinked region of the jet propagates through the standing shock's emission region (gray region), the orientation of the magnetic field with respect to the line of sight changes with time. This change in orientation is parameterized as $\theta'(t)$ in Equation (7). The effects of shock compression, the poloidal magnetic field, and the change in the magnetic pitch angle, $\psi'(t)$, are not shown.

of the $m = 1$ kink mode. The jet's magnetic symmetry axis (parallel to the B_z direction) will then deform into a large-scale helix that is carried with the jet's velocity field (Mizuno et al. 2011), which we assume to be uniform in this work. If the helical deformation passes through a standing shock, as shown in Figure 5, then the magnetic structure of the post-shock region will change in time, thereby producing fluctuations in the post-shock synchrotron emission. Let us further assume that the ratio of B'_ϕ/B'_z varies in time in the post-shock flow. Kink-mode simulations have found that, to avoid total jet disruption, B'_ϕ/B'_z dynamically relaxes to $\sim$1 (Nakamura et al. 2007), while, in competition with this process, jet conical expansion always increases the ratio. Therefore, this competition will produce fluctuations in B'_ϕ/B'_z at the standing shock.

Within this scenario multiple types of disturbances can be envisioned. Herein we consider two. First, we may introduce sinusoidal variations both in the jet frame magnetic pitch angle $\psi' = \tan^{-1}(B'_\phi/B'_z)$ and in the angle between the magnetic symmetry axis and the jet frame line of sight, θ', as shown in Figure 5:

$$\psi'(t) = A'_\psi \sin(\omega_\psi t - \phi_\psi) + \psi'_0 \quad (6)$$

$$\theta'(t) = A'_\theta \sin(\omega_\theta t - \phi_\theta) + \theta'_{ob}, \quad (7)$$

where t is time and $(A'_\theta, A'_\psi, \omega_\theta, \omega_\psi, \phi_\theta, \phi_\psi, \theta'_{ob}, \psi'_0)$ are parameters of the model. The jet frame viewing angle, θ'_{ob}, is actually set by the relation to the observer frame viewing angle by $\sin\theta'_{ob} = \delta \sin\theta_{ob}$. However, as the Doppler factor for the inner jet is unconstrained, θ'_{ob} is treated as a free parameter as long as the required Doppler factor is within reasonable bounds. It should be noted that when the magnetic field passes through the standing shock, the field components lying in the shock plane will be amplified by shock compression. However, this only modifies the form of $\psi'(t)$ and $\theta'(t)$; it does not prevent quasi-periodic variations from occurring.

To calculate the total intensity and fractional polarization from the standing shock, the emission region electron distribution function is assumed to be a power law, $dn = K_e E^{-p} dE$, where the spectral index is related to the electron distribution function by $p = 2\alpha + 1$. We assume that the jet is unresolved and the emission is mostly concentrated in a cylindrical shell centered on the local symmetry axis so that the total intensity and fractional polarization are (Lyutikov et al. 2005)

$$I \approx K(\cos^2\psi' + \cos^2\theta' - 3(\cos\theta'\cos\psi')^2 + 1) \quad (8)$$

$$P \approx \frac{3+3\alpha}{5+3\alpha}\frac{-2(1+3\cos 2\psi')\sin^2\theta'}{5-\cos 2\theta'-\cos 2\psi'-3\cos 2\theta'\cos 2\psi'}, \quad (9)$$

where θ' and ψ' are the variables defined in Equations (7) and (6), respectively, and K is an arbitrary constant that depends on emission region details such as the beaming factor, emission region size, relativistic particle density, and magnetic field strength (Lyutikov et al. 2005). The sign of P indicates whether the EVPA is parallel ($P > 0$) or perpendicular ($P < 0$) to the jet frame local magnetic symmetry axis in the standing shock. At any time t', the values of θ' and ψ' represent the particular orientation of the kinked magnetic field and the value of the magnetic pitch angle in the standing shock, respectively. (See the appendix for a derivation of Equations (8) and (9).)

5.2. Polarization and Spectral Behavior of HST-1: Interpretation

We believe that the most consistent explanation for the variability observed in HST-1 is that the flare occurred in a shock within the jet, with the maximum polarization coming at the time of maximum compression and also maximum optical flux. The high polarization (P at maximum in excess of 40%) and alignment of the EVPA with the jet axis in HST-1, rules out the conical reconfinement hydrodynamic shock model of Nawalejko (2009; see also Bromberg & Levinson 2009). Assuming that the jet magnetic field is weak and tangled, such models cannot produce a polarization higher than $\sim$30%. Furthermore, such a model would predict a substantially different orientation of EVPA for small and intermediate jet inclinations. The EVPA we observe in HST-1 is very nearly perpendicular to the jet, and nearly constant, so a more consistent explanation for the data is that the non-thermal activity is restricted to a localized, perpendicular (possibly stationary) strong shock within the interior of the flow, as envisioned in Section 5.1 (see Equation (1)), which is also more in line with

the observed radio morphology. The feature producing the flare may then be associated with the Mach disk produced around the nozzle (converging point) of the reconfinement shock (Stawarz et al. 2006, Paper IV; Gracia et al. 2009). In the latter model (Gracia et al. 2009), the synchrotron emissivity is proportional to the comoving frame electron density and magnetic field strength and configuration, modulo $\delta^{(2+\alpha)}$, rather than being dependent on hydrodynamic energy dissipation as assumed in Nawalejko (2009).

Using the doubling/halving timescales calculated for the optical/UV emission in Madrid (2009) as well as those in Paper II for the X-ray emission, we can estimate a size of $\leqslant 0.5\delta$ lt-yr (where δ is the Doppler factor) for the size of the flaring region, with the irregularity of the available measurements perhaps arising because of the complexity of the compression mechanism (we do not believe it arises because we did not sample adequately, given the smoothness of the observed light curve). This is consistent with the fact that HST-1 is not resolved by *HST*, which sets a hard upper limit of 2 pc on the radius of the optically emitting components (Paper II, Madrid 2009). Interestingly, however, as already noted in Paper II and Madrid (2009), the X-ray and optical/UV doubling/halving timescales do not lead to significantly different constraints for the region size.

If we then apply Equation (1) to knot HST-1, we can reproduce the type of behavior seen in the (I, P) plane (Figure 3). But equally interestingly, we can also constrain the kinematics in the local flow under certain assumptions. To illustrate, we choose $k = 0.25$, appropriate for a strong relativistic shock (Meisenheimer et al. 1989), spectral index $0.45 \leqslant \alpha \leqslant 0.55$, corresponding to the mean observed during both flare "loops" (Figures 2 and 4) and $0.35 \leqslant P \leqslant 0.45$, consistent with the peak value attained at both flux maxima. We then allow the viewing angle θ_{ob} and Doppler factor δ to vary. We constrain the solutions so that the apparent speed $\beta_{\rm app}$ falls within the range $4.0 < \beta_{\rm app} < 4.5$, the values reported for very long baseline interferometry components in Paper IV. The result is shown in Figure 6. As can be seen, the permitted values of θ_{ob} range between 11° and 18°, and δ can range between 2.5 and 5.5. The Lorentz factor, Γ is more stable, however, with permitted values ranging between 4.1 and 4.8. These values are in agreement with the upper limit of $\delta = 8$ calculated by Waters & Zepf (2005) based on other considerations, and are also consistent with the requirement of $\theta_{ob} < 19°$ from the somewhat faster superluminal speeds seen in *HST* monitoring during the 1990s (Biretta et al. 1999). It should be mentioned that with these values of α, P, and k there are no allowed solutions with $\Gamma < 2$, and moreover, nearly all the allowed solutions with $\Gamma < 3$ require values of $\theta_{ob} > 20°$, which is not allowed.

Interestingly however, we see no evidence for motion of the flaring region of HST-1 in our data, as our astrometric results (all epochs having identical distances between the nucleus and HST-1 to a tolerance of $\pm 0\farcs01$) translate to an upper limit of $1.02c$ (2σ) on motion of the flaring region itself. While this seems to conflict with the VLBA measurements of Paper IV, as well as our calculation of δ from the shock model, this should not be too concerning. It is entirely possible that the flaring region itself represents a standing shock, not flowing along with the plasma. Under such a scenario we could not expect the observed speed to accord with the local jet Lorentz factor. Indeed, the VLBA maps (Paper IV) show a stationary upstream end to the HST-1 region. For most of the time period covered by Paper IV, the observed speeds are consistent with our limit, as the flaring region (component HST-1c in their nomenclature), while downstream from the stationary upstream end (HST-1d), has a speed of $1.14 \pm 0.14c$, measured relative to HST-1d. Beginning around epoch 2006.0, however, HST-1c splits into two components, with the faster, downstream one (accounting for the majority of the radio flux) accelerating to $4.3 \pm 0.7c$ relative to HST-1d. While this latter speed is on the surface highly inconsistent with our astrometric results, it is important to realize that our data are not very sensitive to this time period, as it contains only 5 of our 17 ACS epochs (the lower-resolution WFPC2 observations of epoch 18 are much less useful for astrometry). Using only our ACS data during 2006, the limit on motion of the flaring region would be much less restrictive, i.e., $\sim 5.5c$ at 2σ. Use of later epoch data would improve this result; however, there was a gap in UV monitoring of the M87 jet between late 2006 and mid-2009, a time interval that featured a further factor ~ 5 decrease in the X-ray flux of HST-1 (e.g., Paper V and later data), which could make it very difficult to identify the flaring components. The necessary data do, however, exist in the VLBA archive, and it would be highly interesting to track the motion of the flaring region in both bands.

If indeed the giant HST-1 flare was a result of enhanced particle acceleration occurring within a compressing shock, then it would be logical to ascribe the cooling during the main flare to relaxation of the compression that occurred within the shock. In that case, the energy dependence—or lack thereof—of

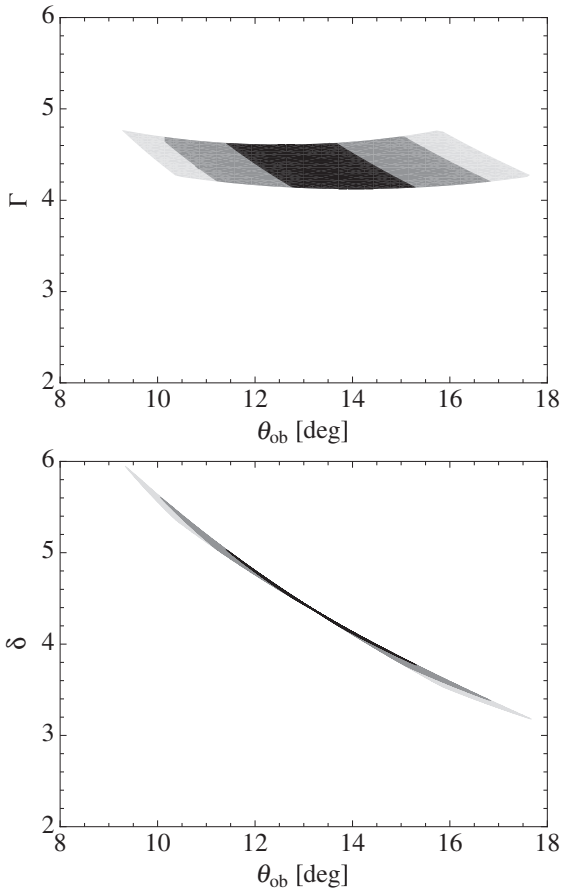

Figure 6. Allowed values of beaming parameters for our shock model of knot HST-1. At top, we show the allowed range for the Lorentz factor Γ and viewing angle θ_{ob}, while at bottom, we show the corresponding range for the Doppler factor δ plotted against viewing angle θ_{ob}. In both panels, light gray colors refer to spectral indices $\alpha = 0.45$, gray colors refer to $\alpha = 0.5$, and black colors refer to $\alpha = 0.55$. See Sections 5.1 and 5.2 for discussion.

the variability timescales (in optical and other bands) may be set by the dynamical timescale of the compression, as originally noted in Paper II and explored further in Paper V and Madrid (2009). For example, if the compression and subsequent expansion were adiabatic, one would expect to see frequency-independent variability behavior unless there was an intrinsic, pre-existing break in the spectrum. This would be modified where the particle cooling and acceleration timescales ($t_{\rm acc}$ and $t_{\rm cool}$, respectively) are equal to or less than the dynamical timescales. As already noted, we observe hard lags in the optical–UV during the brightest part of the flare (epochs 5–9; Figure 4). To explain such hard lags, $t_{\rm acc}$ must be similar to $t_{\rm cool}$, whereas when soft lagging was observed (epochs 13–17), the opposite relationship would hold, i.e., $t_{\rm acc} < t_{\rm cool}$. Interestingly, as shown in Paper V, in both the UV and X-rays the derivative dI/dt changed sign between 2005.4 and 2005.5, i.e., epochs 9 and 10. If indeed this was related to the relationship between the acceleration and cooling timescales, then the oscillations seen in epochs 10–13—which occurred during a time when the flux was decreasing monotonically—become important. The multi-wavelength spectral characteristics of HST-1 discussed above could be possibly explained in the framework of the scenario in which the primary loss mechanism in the optical–UV is Comptonization of external radiation and the optical–UV emitting electrons are near the transition between the Thomson and Klein–Nishina regimes (see the discussion in Section 6 below).

As discussed in Section 4, the mean EVPA in HST-1 is somewhat different from the PA of the jet. Thus while a shock morphology is likely for HST-1, the polarization data hints at a more complex morphology than indicated by the simple, unresolved appearance shown by the images. Two interpretations are possible. The first possibility is that HST-1's optical polarized flux comes from two or more regions. While this might seem the simplest interpretation, it is difficult to reconcile this with the strong correlation between flux and polarization, combined with the constant EVPA. In addition, the unresolved nature of the flaring region in our data and that of Madrid (2009), constrains the maximum separation of these components to $\sim$2 pc, which translates to a constraint on the cooling timescale that, as already discussed, is consistent with the spectral evolution we see. Alternatively, it could indicate either a twist in the field within the shocked region and/or an oblique shock, as suggested for the knot A region by Bicknell & Begelman (1996). In the latter case, one might expect to see evidence of a slight local deviation in the flow direction, and indeed, the VLBA components seen in Paper IV do have a significant range of radius vector PAs as measured from the standing feature at the upstream end of the HST-1 complex. Furthermore, there is weak evidence of small changes in EVPA over time, with the EVPA near the two flux maxima (epochs 8, 9, and 16) being within 2°–3° of the PA of the radial vector from the nucleus to HST-1 from the VLBA data, while in the other 15 epochs the EVPA is more closely aligned with the motion vector of the faintest feature of the HST-1 complex as seen on the VLBA maps, namely, component "a," at the downstream end. Note however that if the shock lies well within the interior of the jet these deviations might not be indicative of an overall deflection of the flow (as in knot A). On a somewhat related note, Nakamura et al. (2010) recently proposed a model for the overall structure of the M87 jet, in which the main shocks in the M87 jet have a helical magnetic field structure, which could be produced via two methods. Bicknell & Begelman (1996) suggested that the knots in the M87 jet are generated by the helical modes, which can produce lateral oscillation of the entire jet but has trouble producing filaments within it. Hardee & Eilek (2011), by contrast, postulate that the elliptical Kelvin—Helmholtz modes dominate and model the inner M87 jet as having twisted, high-pressure filaments generated by elliptical Kelvin–Helmholtz instabilities which eventually disrupt the jet beyond knot A. Assuming that the magnetic field within the components is perpendicular to the local bulk velocity vector (rather than the mean jet axis vector), such a model can produce the slight offset between EVPA and jet PA seen in nearly all of the observations of HST-1.

5.3. Polarization Behavior of the Nucleus: Interpretation

Because the polarization and flux variability of the nucleus forms a coherent pattern—a counterclockwise loop in $I - P$ space, over the course of a year—the available data challenge scenarios where the variability of the nucleus is dominated by multiple independent components. The most natural interpretation of the nuclear polarization variability is that within the small aperture chosen (which represented approximately two *HST* resolution elements) the structure of the M87 jet is relatively simple, perhaps having a single region of the jet dominating the flux and polarization variability at any one time. This scenario is consistent with either models of a magnetically dominated jet in which large-scale magnetohydrodynamic instabilities play an important role (e.g., Giannios & Spruit 2006) or with models of a non-stationary flow through a standing shock. Within such a model there are a number of ways to explain the behavior seen in the nucleus. In Section 5.1, we have illustrated two possible scenarios that may occur—namely, either (1) there is a standing shock through which a time-varying flow propagates, or (2) the jet contains a large-scale helical field subject to the kink mode in a region of a standing shock as shown in Figure 5. Both of these possibilities (see the discussions surrounding Equations (2)–(5) and (6)–(9), respectively) are motivated by (1) the variability of jet flow speeds as seen in superluminal studies of jets and (2) the prominence of the kink mode in theoretical analyses of magnetically dominated jets, respectively.

The two scenarios considered here each produce different tracks in the (I, P) plane. In Figure 7, we show an example track for each, assuming a viewing angle $\theta_{ob} = 15°$, consistent with the observation of superluminal motions at speeds as high as $6c$ in HST-1 (Biretta et al. 1999, Paper IV; see also Section 5.2). As shown, both scenarios successfully reproduce two general characteristics of the looping behavior we see in the (I, P) plane between epochs 6 to 15 in Figure 3, namely: (1) successive points are located close together in (I, P) space and (2) these points form a coherent pattern (a loop) over the course of a $\sim$ year as shown in figure 7. Nonetheless, both models suffer from shortcomings. Constraining the shock compression model to produce EVPAs parallel to the jet direction severely restricts the maximum polarization it can achieve. Thus, the model's maximum polarization reaches only $\sim$6%, while the observations achieve a maximum of $\sim$11%. In the helical distortion model, maintaining a low polarization and producing an EVPA parallel to the jet implies restricting the variability of the magnetic pitch angle to be $\psi' = 1/2\cos^{-1}(-1/3) + \epsilon$, where $0 < \epsilon \ll 1$, which is an arbitrary constraints on the oscillation of ψ'. More generally, both models are limited by their extreme simplicity (e.g., neither have sheared velocity fields), high number of free parameters, and non-uniqueness.

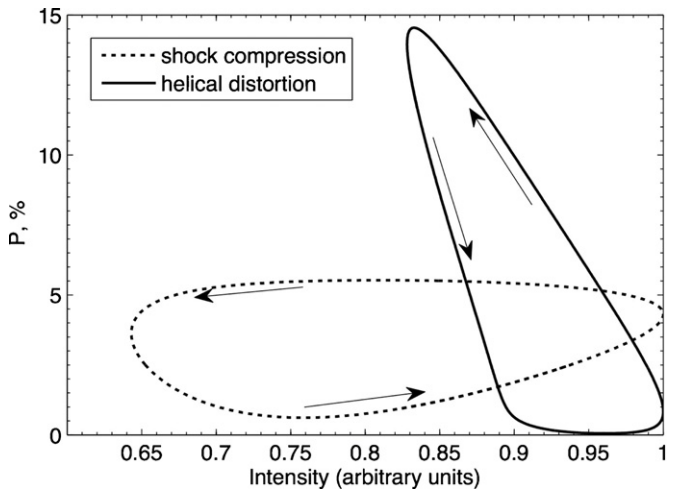

Figure 7. Illustrated here is a theoretical counterclockwise $I - P$ loop for the helical distortion model (solid) and the variable shock compression model (dotted). The values used in the shock compression model are $(\beta_{u,0}, A_\beta, \omega_\beta, \phi_\beta) = (0.78, 0.03, 1, -\pi/2)$ and $(\xi_0, A_\xi, \omega_\xi, \phi_\xi) = (0.78, -0.5, 1, 0)$. For the helical distortion model, $(A'_\theta, \omega_\theta, \phi_\theta, \theta'_{ob}) = (1.5, 1, 0, \pi/2)$ and $(A'_\psi, \omega_\psi, \phi_\psi, \psi'_0) = (0.05, 2, 0, 1.03)$ and $\delta = \sin\theta'_{ob}/\sin 15^\circ \approx 3.86$. For both models, $\theta_{ob} = 15^\circ$ and $\alpha = 1.5$ were used.

Of the two toy models discussed herein, we would argue that the (I, P) behavior we observe (Figure 3) is closer to that produced by the helical distortion model, although again, neither model reproduces the observed behavior perfectly. The shock compression model requires a roughly linear increase of polarization with flux in its "positive" stage, followed by a "plateau" with polarization nearly constant at its maximum while the flux decreases. Neither of these is observed in the nucleus. Instead, we see very steep increases in polarization during epochs 6–9 (from 2% up to 12%), while the flux changes are much smaller. The pattern does not exactly reproduce what is seen in the helical distortion model either, however. Local maxima in flux are seen at epochs 7 and 12. Of these, the former corresponds to a local maximum in P while the latter does not; indeed, the global maximum in P comes at epoch 9, when the flux is declining. In fact, one could actually argue that a "plateau" is seen between epochs 9 and 10, as the two polarization measurement are statistically indistinguishable from one another while the fluxes differ by 25%. It is possible that both types of variations are seen, somewhat out of phase with one another, but while this is plausible such a model would produce competing variations that are difficult to model without introducing ad hoc assumptions.

Neither of these models is fully successful in reproducing the EVPA fluctuations we observe (Figure 1). The helical distortion model predicts that the EVPA time evolution should correlate with the polarization and intensity. We expect this correlation because the helical distortion flowing through the standing shock causes the orientation of the magnetic field symmetry axis in the post-shock flow to fluctuate as illustrated in Figure 5; in turn, the post-shock flow EVPA, intensity, and polarization depend on the fluctuating field geometry. Unlike the helical distortion model, the varying shock compression model maintains cylindrical symmetry even as other parameters vary with time. Thus, the shock model predicts the EVPA should remain stationary or undergo rapid 90° flips. It should be noted, however, that the dominant observed EVPA of the nucleus is close to parallel to the jet, an orientation which both toy models reproduce for the parameters used in Figure 7.

The lack of variability we observe in $\alpha_{\rm O-UV}$ for the nucleus ostensibly fits better within the helical distortion than with the shock compression model. In the helical distortion model, the shock strength and particle distribution parameters, K_e and p $(= 2\alpha + 1)$, are held constant and only the magnetic geometry fluctuates, hence the lack of spectral index variation in the model. However, more realistically, in particle acceleration models such as diffusive shock acceleration (or first-order Fermi acceleration), the particle acceleration efficiency depends on the angle between the large-scale magnetic field and the shock plane (Sironi & Spitkovsky 2011). In the case of the shock compression model, the increased shock compression ratio leads to enhanced particle acceleration, as envisioned in Section 5.2 for HST-1, the expectation is a strong correlation between flux and $\alpha_{\rm UV-O}$, either hard or soft lagging depending on the relationship between the acceleration and cooling timescales.

6. SUMMARY

This work has revealed the value of polarization and spectral information in monitoring campaigns, as well as in understanding the physics of jet regions. We have shown that knot HST-1 can be best understood as a shocked region, where the flaring upstream end did not move significantly between 2002 and 2007 and displays characteristics that are consistent with a classic perpendicular shock. Under such a model we find that the Lorentz factor in the jet at HST-1 can be constrained to a fairly narrow range, $4.1 \leqslant \Gamma \leqslant 4.8$, and the viewing angle can also be constrained to $10^\circ \leqslant \theta_{ob} \leqslant 18^\circ$. The optically emitting part of the jet within HST-1 may well contain multiple components (as the radio emitting part does, see Paper IV), given the fine points of the EVPA structure (Section 5.2); however the *HST* data do not have the angular resolution to resolve this region. The spectral behavior of HST-1 was consistent with nearly equal particle acceleration and cooling timescales in the optical–UV; however, the fact that the X-ray emission is best understood as synchrotron radiation complicates things. Two interpretations are possible for this duality. The first of these is that the X-ray emission may come from a small part of the jet in HST-1 (as suggested for downstream regions of the jet by Perlman & Wilson 2005), which may either be partially cospatial with the optical emission region or distinct from it. This interpretation is disfavored, however, because of the overall similar appearance of the UV and X-ray light curves (Paper V). A more likely interpretation is that, while the likely emission mechanism in both bands remains synchrotron radiation, the dominant energy loss mechanism is inverse-Comptonization of external radiation, with the X-ray emitting electrons being in the Klein–Nishina regime, while the optical/UV emitting electrons are either in the Thomson regime or around the Thomson/Klein–Nishina transition. Under such a scenario the cooling timescale of lower-energy optical–UV photons may be comparable to or shorter than the cooling timescale of X-ray emitting electrons. The flat optical spectra observed in HST-1 ($\alpha \lesssim 0.5$) are in fact very consistent with such an idea (Moderski et al. 2005). In such a scenario the inverse-Compton emission would dominate at higher energies and in fact would be energetically dominant when integrated over the entire electromagnetic spectrum. This would be consistent with the correlation of the 2005 TeV flare with the HST-1 flare seen at lower energies (Abramowski et al. 2011).

The variability behavior seen in the nucleus, however, can be best understood as either a helical distortion to a steady jet, where the distortion would arise from kink mode instabilities, or fluctuations in the jet speed that produce corresponding

fluctuations in the strength of shocks within the nuclear jet. Both of these toy models can produce the fluctuations in field components that can result in the "looping" polarization behavior we see. We believe the most likely mechanism is a current-driven instability combined with a fluctuating, helical magnetic pitch angle. Jet precession can be ruled out as there is no evidence of jet wobbles on larger resolved scales. This leaves large-scale instabilities as a possible cause of the wobbling axes. Kelvin–Helmholtz instabilities could cause the wobbling; however these are important in hydrodynamic jets and as discussed in Section 5.3 we believe that in the nuclear regions the M87 jet is more likely to be magnetically dominated, with a helical magnetic field structure. The kinked jet scenario naturally leads to magnetic pitch angle fluctuations. Future monitoring of the variability behavior of spatially resolved jets should include both multi-band imaging and polarimetry on the same timescale in order to maximize the physical information that can be gained from the campaign.

We thank an anonymous referee for thoughtful comments that significantly improved the quality of this paper. E.S.P., M.G., M.C., and R.C.S. acknowledge support from NASA under LTSA program Grant NNX07AM17G and HST Grant GO-11138.01. E.C. acknowledges support from the NASA *Fermi* Grant NNX10AO46G. S.C.A. and M.B. acknowledge SARA REU fellowships, funded by the National Science Foundation Research Experiences for Undergraduates (REU) program through grant NSF AST-1004872. E.S.P. acknowledges interesting discussions with L. Sironi and M. Birkinshaw which helped with understanding the variability behavior we see.

APPENDIX

HELICAL FIELD INTENSITY AND POLARIZATION

Here we derive the expressions for synchrotron intensity (Equation (8)) and polarization (Equation (9)) of an unresolved jet with an emitting cylindrical shell containing a helical field, a configuration first considered in the nonrelativistic case by (Laing 1981). The notation and discussion here follows that of Lyutikov et al. (2005), who explicitly derive the polarization expression in their Equation (21). The synchrotron intensity and polarization can be expressed as integrals over the entire cylindrical shell:

$$I = K \int_0^{2\pi} \left| B' \sin \chi' \right|^{\alpha+1} d\phi \tag{A1}$$

$$P = \frac{3+3\alpha}{5+3\alpha} \frac{\int_0^{2\pi} |B' \sin \chi'|^{\alpha+1} \cos 2\tilde{\chi} d\phi}{\int_0^{2\pi} |B' \sin \chi'|^{\alpha+1} d\phi}, \tag{A2}$$

where ϕ is the azimuthal cylindrical coordinate, K is a constant, χ' is the angle between the jet frame line of sight and the jet frame magnetic field, and $\tilde{\chi}$ is the angle between the EVPA and the jet's projected onto the sky, measured clockwise. To obtain analytical results, we assume $\alpha = 1$ in carrying out the above integration.

Assume a Cartesian coordinate system centered on the jet with the bulk flow directed along the z-axis and with the observer in the $y = 0$ plane. Therefore, the jet velocity is

$$\vec{\beta} = \beta(0, 0, 1) \tag{A3}$$

and the photon propagation vector is

$$\hat{n} = (\sin \theta_{ob}, 0, \cos \theta_{ob}). \tag{A4}$$

The jet frame shell magnetic field unit vector has a pitch angle of $\tan \psi' = B'_\phi / B'_z$ and can be expressed in cylindrical coordinates as

$$\hat{B}' = (-\sin \psi' \sin \phi, \sin \psi' \cos \phi, \cos \psi'). \tag{A5}$$

Thus, $\sin \chi' = \vec{n}' \cdot \hat{B}'$ can now be expressed as

$$\sin^2 \chi' = \cos^2 \psi' \sin^2 \theta'_{ob} + \frac{1}{2} \sin 2\theta'_{ob} \sin 2\psi' \sin \phi + (\cos^2 \theta'_{ob} + \cos^2 \phi \sin^2 \theta_{ob}) \sin^2 \psi'. \tag{A6}$$

Integrating this expression over ϕ for $\alpha = 1$ produces the intensity

$$I = K(\cos^2 \psi' + \cos^2 \theta'_{ob} - 3(\cos \theta'_{ob} \cos \psi')^2 + 1). \tag{A7}$$

To find the polarization, all that remains to be calculated is $\cos 2\tilde{\chi}$. First, note that the polarization vector of a synchrotron electromagnetic wave in the jet frame is $\hat{e}' = \vec{n}' \times \hat{B}'$. $\tilde{\chi}$ may now be written as

$$\cos \tilde{\chi}' = \hat{e}' \cdot (\vec{n}' \times \vec{\ell}), \tag{A8}$$

where $\vec{n}' \times \vec{\ell}$ is the jet direction projected onto the sky and $\vec{\ell} = (0, 1, 0)$ in Cartesian coordinates. Evaluating $\cos \tilde{\chi}'$ leads to

$$\cos 2\tilde{\chi}' = \frac{\cos^2 \phi \sin^2 \psi' - (\cos \psi' \sin \theta'_{ob} + \cos \theta'_{ob} \sin \phi \sin \psi')^2}{1 - (\cos \psi' \cos \theta'_{ob} - \sin \theta'_{ob} \sin \phi \sin \psi')^2}. \tag{A9}$$

Therefore, according to Equation (A2),

$$P = \frac{3/2(1 + 3\cos 2\psi') \sin^2 \theta'_{ob}}{5 - \cos 2\theta'_{ob} - \cos 2\psi' - 3 \cos \theta'_{ob} \cos 2\psi'}. \tag{A10}$$

Note that Equations (A6) and (A9) are Equations (20) of Lyutikov et al. (2005). Although this result strictly holds for $\alpha = 1$, it can be extended to other values close to $\alpha = 1$ by the following analytic approximation

$$P = \left(\frac{3+3\alpha}{5+3\alpha}\right) \frac{2(1 + 3\cos 2\psi') \sin^2 \theta'_{ob}}{5 - \cos 2\theta'_{ob} - \cos 2\psi' - 3 \cos \theta'_{ob} \cos 2\psi'}. \tag{A11}$$

REFERENCES

Abdo, A., Ackermann, M., Ajello, M., et al. 2009, ApJ, 707, 55
Abramowski, A., et al. 2011, ApJ, submitted
Aharonian, F., Akhperjanian, A., Beilicke, M., et al. 2003, A&A, 403, L1
Aharonian, F., Akhperjanian, A. G., Bazer-Bachi, A. R., et al. 2006, Science, 314, 1424
Asada, K., Inoue, M., Uchida, Y., et al. 2002, PASJ, 54, L39
Begelman, M. C. 1998, ApJ, 493, 291
Bicknell, G. V., & Begelman, M. C. 1996, ApJ, 467, 597
Biretta, J. A., & McMaster, M. 1997, WFPC2 Polarization Calibration Handbook, WFPC2 Instrument Science Report 1997-11 (Baltimore, MD: STScI)
Biretta, J. A., Sparks, W. B., & Macchetto, F. D. 1999, ApJ, 520, 621
Bohlin, R. C. 2007, Instrument Science Report ACS 2007-06
Bromberg, O., & Levinson, A. 2009, ApJ, 699, 1274
Chen, Y. J., Zhao, G. Y., & Shen, Z. Q. 2011, MNRAS, 416, L109
Cheung, C. C., Harris, D. E., & Stawarz, L. 2007, ApJ, 663, L65
Clausen-Brown, E., Lyutikov, M., & Kharb, P. 2011, MNRAS, 415, 2081
Curtis, H. D. 1918, Pub. Lick Obs., 13, 9
Fiorucci, M., Ciprini, S., & Tosti, G. 2004, A&A, 419, 25

Fruchter, A., & Sosey, M. 2009, The MultiDrizzle Handbook version 3.0 (Baltimore, MD: STScI)
Gabuzda, D. C., Murray, É, & Cronin, P. 2004, MNRAS, 351, L89
Giannios, D., & Spruit, H. C. 2006, A&A, 450, 887
Gracia, J., Vlahakis, N., Agudo, I., Tsinganos, K., & Bogovalev, S. V. 2009, ApJ, 695, 503
Hardee, P. E., & Eilek, J. A. 2011, ApJ, 735, 61
Harris, D. E., Biretta, J. A., Junor, W., et al. 2003, ApJ, 586, L41
Harris, D. E., Cheung, C. C., Biretta, J. A., et al. 2006, ApJ, 640, 211
Harris, D. E., Cheung, C. C., Stawarz, L., Biretta, J. A., & Perlman, E. S. 2009, ApJ, 699, 305
Hook, R. N., Walsh, J., Pirzkal, N., & Freudling, W. 2000, in ASP Conf. Ser. 216, Astronomical Data Analysis & Software Systems IX, ed. N. Manset, C. Veillet, & D. Crabtree (San Francisco, CA: ASP), 671
Hughes, P. A., Aller, H. D., & Aller, M. F. 1985, ApJ, 298, 301
Kharb, P., Gabuzda, D. C., O'Dea, C. P., Shastri, P., & Baum, S. A. 2009, ApJ, 694, 1485
Kollgaard, R. I., Wardle, J. F. C., & Roberts, D. H. 1990, AJ, 100, 1057
Laing, R. A. 1980, MNRAS, 193, 439
Laing, R. A. 1981, ApJ, 248, 67
Landau, L. D., & Lifshitz, E. M. 1987, in Fluid Mechanics (Oxford: Pergamon)
Lind, K. R., & Blandford, R. D. 1985, ApJ, 295, 358
Lister, M., Cohen, M. H., Homan, D. C., et al. 2009, AJ, 138, 1874
Lyutikov, M., Pariev, V. I., & Gabuzda, D. C. 2005, MNRAS, 360, 869
Madrid, J. M. 2009, AJ, 137, 3864
Marscher, A. P. 2009, in The Jet Paradigm: From Microquasars to Quasars, ed. T. Belloni (Lecture Notes in Physics, Vol. 794; Berlin: Springer), arXiv:0909.2576
Maybhate, A., et al. 2010, ACS Instrument Handbook
Meisenheimer, K., Röser, H.–J., Hiltner, P. R., et al. 1989, A&A, 219, 63
Moderski, R., Sikora, M., Coppi, P. S., & Aharonian, F. 2005, MNRAS, 363, 954
Mizuno, Y., Hardee, P. E., & Nishikawa, K. I. 2011, ApJ, 734, 19
Mobasher, B. 2002, HST Wide Field and Planetary Camera 2 Data Handbook (Baltimore, MD: STScI)
Naghizadeh-Khouei, J., & Clarke, D. 1993, A&A, 274, 968
Nakamura, M., Garofalo, D., & Meier, D. L. 2010, ApJ, 721, 1783
Nakamura, M., Li, H., & Li, S.–T. 2007, ApJ, 656, 721
Nawalejko, K. 2009, MNRAS, 395, 524
Narayan, R., Li, J., & Tchekhovskoy, A. 2009, ApJ, 697, 1681
Perlman, E. S., Biretta, J. A., Sparks, W. B., Macchetto, F. D., & Leahy, J. P. 2001, ApJ, 551, 206
Perlman, E. S., Biretta, J. A., Zhou, F., Sparks, W. B., & Macchetto, F. D. 1999, AJ, 117, 2185
Perlman, E. S., Harris, D. E., Biretta, J. A., Sparks, W. B., & Macchetto, F. D. 2003, ApJ, 599, L65
Perlman, E. S., Padgett, C. A., Georganopoulos, M., et al. 2006, ApJ, 651, 735
Perlman, E. S., & Wilson, A. S. 2005, ApJ, 627, 140
Serkowski, K. 1962, Adv. Astron. Astrophys., 1, 289
Sirianni, M., Jee, M. J., Benítez, N., et al. 2005, PASP, 117, 1049
Sironi, L., & Spitkovsky, A. 2011, ApJ, 726, 75
Spruit, H. C. 2010, in The Jet Paradigm: From Microquasars to Quasars, ed. T. Belloni (Lecture Notes in Physics, Vol. 794; Berlin: Springer), 233 (arXiv:0804.3096)
Spruit, H. C., Foglizzo, T., & Stehle, R. 1997, MNRAS, 288, 333
Stawarz, L., Aharonian, F., Kataoka, J., et al. 2006, MNRAS, 370, 981
Tonry, J. L. 1991, ApJ, 373, L1
Vlahakis, N., & Königl, A. 2004, ApJ, 605, 656
Wardle, J. F. C., Cawthorne, T. V., Roberts, D. W., & Brown, L. F. 1994, ApJ, 437, 122
Wardle, J. F. C., & Kronberg, P. P. 1974, ApJ, 194, 249
Waters, C., & Zepf, S. 2005, ApJ, 624, 656
Zavala, R. T., & Taylor, G. B. 2005, ApJ, 626, L73
Zhang, Y.-H. 2002, MNRAS, 337, 609
Zhang, Y.-H., Beilicke, M., Davies, F., et al. 2002, ApJ, 572, 762